Geophys. J. Int. (2004) **158,** 1103–1117 doi: 10.1111/j.1365-246X.2004.02378.x

The global short-period wavefield modelled with a Monte Carlo seismic phonon method

Peter M. Shearer[1] and Paul S. Earle[2]

[1] *Institute of Geophysics and Planetary Physics, U.C. San Diego, La Jolla,* CA 92093-0225, *USA. E-mail: pshearer@ucsd.edu*
[2] *United States Geological Survey,* MS 966 DFC, PO Box 25046, *Denver,* CO 80225, *USA. E-mail: pearle@usgs.gov*

Accepted 2004 June 8. Received 2004 May 13; in original form 2004 January 28

SUMMARY

At high frequencies (∼1 Hz), much of the seismic energy arriving at teleseismic distances is not found in the main phases (e.g. *P*, *PP*, *S*, etc.) but is contained in the extended coda that follows these arrivals. This coda results from scattering off small-scale velocity and density perturbations within the crust and mantle and contains valuable information regarding the depth dependence and strength of this heterogeneity as well as the relative importance of intrinsic versus scattering attenuation. Most analyses of seismic coda to date have concentrated on *S*-wave coda generated from lithospheric scattering for events recorded at local and regional distances. Here, we examine the globally averaged vertical-component, 1-Hz wavefield ($>10^\circ$ range) for earthquakes recorded in the IRIS FARM archive from 1990 to 1999. We apply an envelope-function stacking technique to image the average time–distance behavior of the wavefield for both shallow ($\leq$50 km) and deep ($\geq$500 km) earthquakes. Unlike regional records, our images are dominated by *P* and *P* coda owing to the large effect of attenuation on *PP* and *S* at high frequencies. Modelling our results is complicated by the need to include a variety of ray paths, the likely contributions of multiple scattering and the possible importance of *P*-to-*S* and *S*-to-*P* scattering. We adopt a stochastic, particle-based approach in which millions of seismic phonons are randomly sprayed from the source and tracked through the Earth. Each phonon represents an energy packet that travels along the appropriate ray path until it is affected by a discontinuity or a scatterer. Discontinuities are modelled by treating the energy normalized reflection and transmission coefficients as probabilities. Scattering probabilities and scattering angles are computed in a similar fashion, assuming random velocity and density perturbations characterized by an exponential autocorrelation function. Intrinsic attenuation is included by reducing the energy contained in each particle as an appropriate function of traveltime. We find that most scattering occurs in the lithosphere and upper mantle, as previous results have indicated, but that some lower-mantle scattering is likely also required. A model with 3 to 4 per cent rms velocity heterogeneity at 4-km scale length in the upper mantle and 0.5 per cent rms velocity heterogeneity at 8-km scale length in the lower mantle (with intrinsic attenuation of $Q_\alpha = 450$ above 200 km depth and $Q_\alpha = 2500$ below 200 km) provides a reasonable fit to both the shallow- and deep-earthquake observations, although many trade-offs exist between the scale length, depth extent and strength of the heterogeneity.

Key words: scattering, seismic coda, seismic wave propagation.

1 INTRODUCTION

The character of the seismic wavefield observed at teleseismic distances ($>30^\circ$) is a strong function of the observation frequency. At low frequencies ($\leq$0.1 Hz) the body wave phases are seen as distinct pulses with little energy between arrivals. These seismograms can be modelled deterministically with specific models of Earth structure. At high frequencies ($\geq$0.5 Hz), an extended coda follows and, in some cases, precedes the main phases. This coda results from scattering off small-scale heterogeneities in the Earth. The coda energy is generally incoherent and is modelled with statistical scattering theories based on random media models.

Aki (1969) and Aki & Chouet (1975) first described how coda observations could be used to estimate the strength of random heterogeneity in the Earth. The ensuing decades have led to a wide variety of observational, theoretical and numerical studies of seismic coda and scattering processes. A comprehensive review of this work is provided in the book by Sato & Fehler (1998; hereafter referred

to as S&F). Particular attention has focused on *S*-wave coda from local and regional earthquakes: this coda often dominates records of these events as a result of strong scattering in the lithosphere. The relatively intense scattering in the crust and upper mantle hampers efforts to resolve possible weaker scattering contributions to the coda from the deeper mantle. However, determining whether such deep scattering exists is important for resolving the heterogeneity structure of the deep Earth at scale lengths much shorter than can be resolved using traveltime tomography.

Evidence for small-scale scattering near the core–mantle boundary (CMB) was noted by Cleary & Haddon (1972) who provided the first correct explanation for the origin of *PKP* precursors. These precursors result from the unusual ray geometry of *PKP*, which permits deep scattered energy to sometimes arrive before the main *PKP* phase, uncontaminated by near-surface scattering. A global study of *PKP* precursors by Hedlin *et al.* (1997) suggested that precursor amplitudes are best explained by whole-mantle scattering, rather than models in which the scattering is confined to the CMB or D″ regions at the base of the mantle, a result supported by the recent *PKP* precursor analysis of Margerin & Nolet (2003b). However, *PKP* precursors sample only approximately 1000 km above the CMB and are observed only over a small range of source–receiver distances. Considering the limited distribution of available seismic sources and receivers, a fairly small fraction of the mantle is actually sampled by *PKP* precursor observations (see, for example, Hedlin & Shearer 2000). Some support for the whole-mantle scattering model was provided by Earle & Shearer (2001) who modelled observations of P_{diff} coda with a single-scattering theory. However, they could not exclude the possibility that multiple scattering near the CMB could also explain the observations. Recently, Lee *et al.* (2003) identified significant lower-mantle scattering from radiative transfer modelling of *ScS* coda.

Our goal in this paper is to present and model the complete global high-frequency seismic wavefield and attempt to resolve the depth dependence of mantle scattering. Rather than examine individual seismograms, we stack and average the data to image the overall time and distance dependence of the arriving energy. These stacks show a large difference between shallow- and deep-event *P* coda, suggesting that the bulk of the *P* coda for shallow events is generated near the source rather than near the receiver. We develop a Monte Carlo, particle-based method to model the data stacks using ray theory to connect scattering events whose probabilities are assigned using theoretical results for random media. This method is energy conserving by design and can handle multiple scattering, conversions between *P* and *S*, and intrinsic attenuation. We achieve good fits to the data stacks with models in which most of the scattering occurs in the upper mantle, as previous results have indicated, but find that some lower-mantle scattering is also required.

2 DATA STACKS

We apply an envelope-function stacking technique to image the global high-frequency wavefield. Unlike most stacking algorithms, the technique allows the imaging of high-frequency scattered waves that are incoherent between seismograms. We used a similar technique in previous studies to characterize high-frequency precursory arrivals to *PKP* and *PKKP* (e.g. Earle & Shearer 1997; Hedlin *et al.* 1997).

To generate stacks with minimal noise contamination, we select a set of high-quality seismograms from the broad-band, vertical-component seismograms stored in the IRIS FARM archive. We use data in the distance range 10° to 100° from earthquakes occurring from 1990 to 1999. Only events with M_W between 6 and 7 are used to provide good signal-to-noise ratios and exclude earthquakes with long source durations. In order to reduce *P* coda contamination, traces containing large aftershocks or contaminating arrivals from earthquakes near the station are removed. We improve the signal content by removing traces with *P*-wave signal-to-noise ratios less than 4 and those with obvious glitches. This culling process resulted in 7591 stackable traces for shallow events (depth $\leq$50 km) and 687 traces for deep events (depth $\geq$400 km). The number of stackable traces could be increased by lowering the magnitude threshold. However, the envelope stacks for the depth ranges considered here are remarkably stable. Differences between stacks generated using independent halves of the data set are small enough to make no difference in our modelling results.

To characterize the average scattered wavefield, we stack the data as follows.

(i) The traces are bandpass filtered between 0.5 and 2.5 Hz. This frequency band falls in a low region of the noise spectrum and provides the greatest sensitivity to deep-Earth structure with a scale-length of approximately 10 km.

(ii) The envelope function (e.g. Kanasewich 1981) is calculated for each seismogram. Using rectified seismograms avoids cancellation of incoherent arrivals when the data are stacked.

(iii) The average noise in a 25-s time window starting 60 s before the theoretical *P* arrival time is subtracted from the envelope function and the trace is normalized to the maximum *P* amplitude. This accounts for varying signal and noise levels between traces.

(iv) The processed seismograms are aligned on the predicted *P* onset, binned in distance and time (5°, 2 s) and the average value is calculated and plotted. To avoid complications resulting from depth phases, separate stacks are made for shallow and deep events. (Figs 1 and 2).

In these stacks, the *P* waves have been normalized to the same amplitude in order to image properly the coda among events of varying sizes. Thus, absolute amplitude versus range information has been lost. To examine the amplitudes, we separately process the peak amplitudes from the individual seismograms (filtered) that go into the stacks. The results, following corrections for instrument gain and event magnitude, and empirical corrections for station terms, are plotted for shallow events in Fig. 3. Amplitudes drop sharply within the 20° and 30° range, fall off gradually from 30° to 85° and then fall off more steeply beyond 85°. These results are similar to the depth–distance corrections that are applied in computing m_b magnitudes from *P*-wave amplitudes and are in reasonable agreement with plots in Veith & Clawson (1972). Our purpose in including them here is to provide amplitude versus range constraints for our modelling efforts.

Our analysis will concentrate on the coda between *P* and *PP*, where most of the scattered energy in these images arrives. Fig. 4 compares the shallow- and deep-event stacks at times up to 300 s following the direct *P*-wave arrival. This figure illustrates the markedly different character of the *P* coda between shallow and deep events. The shallow-event coda is much more energetic and long-lasting than the deep-event coda. For example, at 50 s following the *P* arrival, it is 2 to 5 times larger in amplitude (4 to 25 times larger in energy). This difference is much too large to be explained by any systematic variation in the source duration between shallow and deep events. Instead, it indicates that the bulk of the *P* coda from shallow events is caused by near-source scattering above 600 km depth. Note that both stacks should have comparable coda

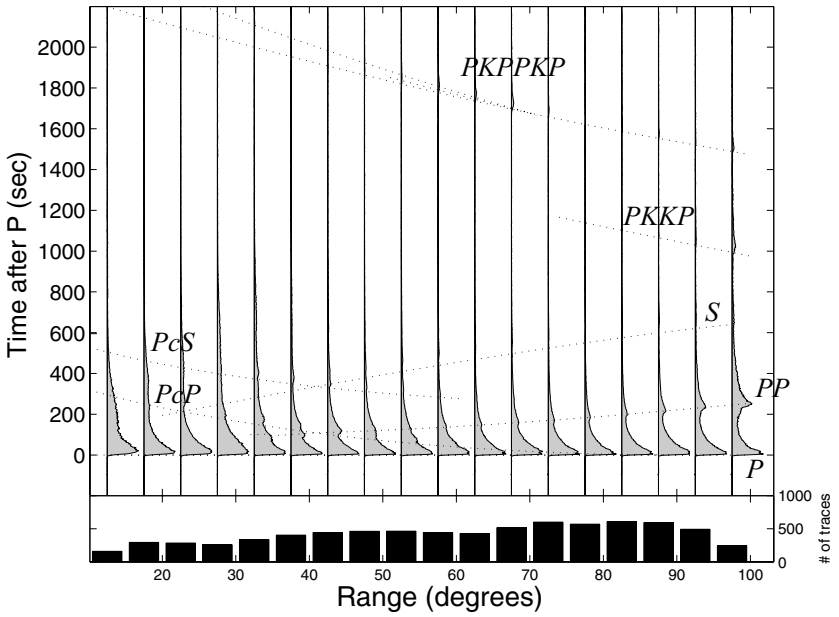

Figure 1. Envelope-function stack of shallow events (less than 50 km depth) between 1990 and 1999 as retrieved from the IRIS FARM archive. Traces are filtered to between 0.5 and 2 Hz and normalized to unit *P*-wave amplitude prior to stacking. The number of seismograms that are summed within each 5° distance bin is shown below, for a total of 7591 traces. Time is relative to the theoretical direct *P* arrival. Other seismic phases are plotted as dotted lines, including the surface reflected *PP* phase and the core phases *PKKP* and *PKPPKP*.

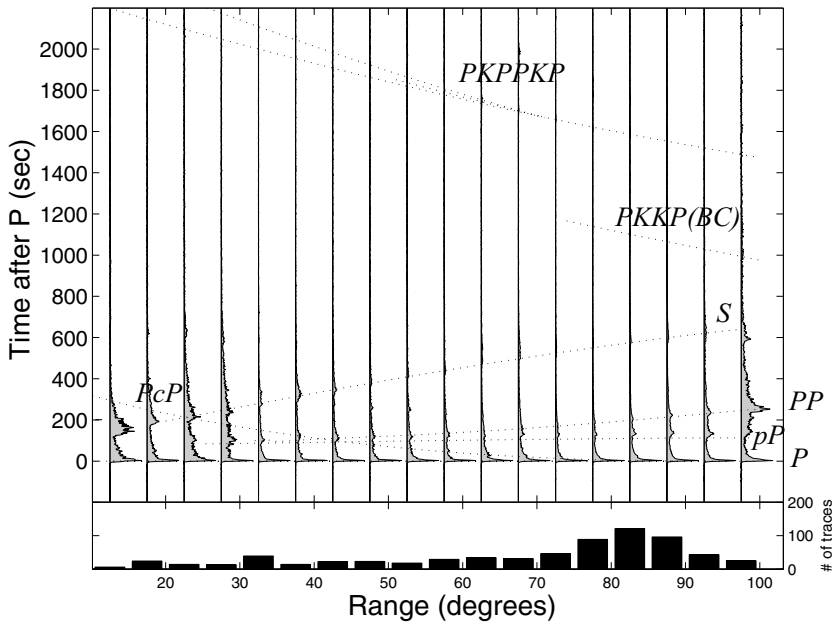

Figure 2. Envelope-function stack of 687 seismograms from deep events (more than 400 km depth) between 1990 and 1999 as retrieved from the IRIS FARM archive. See Fig. 1 caption for other plot details. Note that the *P* coda amplitude is much less than in the shallow-event stack.

contributions from near-receiver scattering, but that the energy difference between the shallow and deep coda is much more than the factor of 2 that simple source–receiver reciprocity arguments might imply for 1-D models. In fact, there is no reason to expect equal contributions to the coda in this case. The sources radiate both *P* and *S* waves; near-source *S*-to-*P* conversions will contribute significantly to the *P* coda while near-receiver *S*-to-*P* conversions will be much less important because of the large attenuation of the *S* waves as they travel through the mantle. As we will show later, it is possible to achieve a reasonable fit to both the shallow- and deep-earthquake coda amplitudes with a single model in which scattering strength varies only with depth.

3 SEISMIC PHONON METHOD

A variety of approaches to modelling scattered waves have been developed, including single-scattering (Born) theory, multiple-scattering theories, diffusion equation approaches for strong scattering regimes and radiative transfer theories. Comprehensive reviews

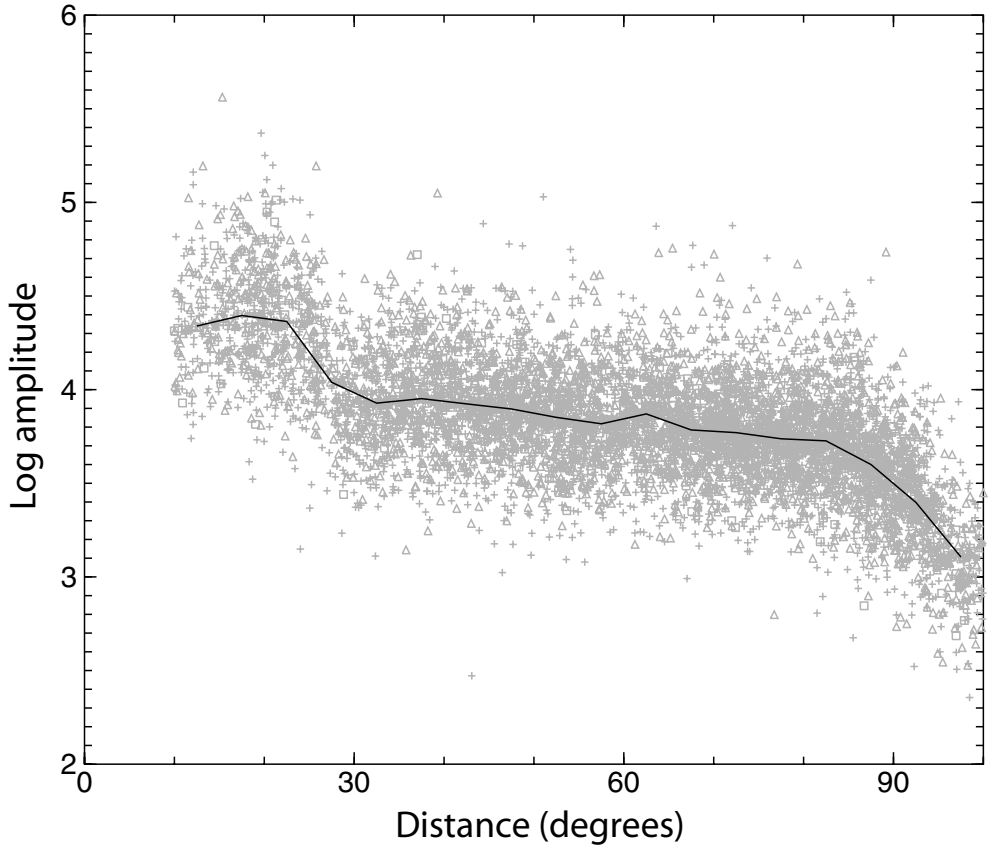

Figure 3. *P*-wave amplitude versus range for the individual seismograms used in the shallow-event, envelope-function stack of Fig. 1. The line shows the median amplitude in 5° bins. Empirical source and receiver corrections have been applied. Amplitude units are arbitrary. Note the relatively gradual decay of amplitude with distance between 30° and 80°.

of these methods are contained in S&F. For modelling our short-period wavefield stacks, we have adopted a Monte Carlo, particle-based approach in which the computer is used to spray millions of seismic phonons from the source, which are then randomly scattered using probabilities computed from random media theories. Various versions of this approach are described by Gusev & Abubakirov (1987), Hoshiba (1991, 1994, 1997), Margerin *et al.* (2000), Yoshimoto (2000) and Margerin & Nolet (2003a,b). This method is attractive for modelling our data because energy conservation is guaranteed, single and multiple scattering are naturally generated, intrinsic attenuation is easily included and both *P* and *S* waves can be modelled. The method is based on ray theory and shares many of the common advantages (computation speed) and disadvantages (inaccurate results in some situations, e.g. core diffracted waves) of ray theoretical approaches.

In describing the specifics of how our particular algorithm works, we will use the appropriate equations from S&F to which the reader is referred for more details (see also Wu 1985; Wu & Aki 1985a,b). We assume that *P* velocity α and *S* velocity β have the same fractional velocity fluctuations (S&F equation 4.47):

$$\xi(\mathbf{x}) = \frac{\delta\alpha(\mathbf{x})}{\alpha_0} = \frac{\delta\beta(\mathbf{x})}{\beta_0}, \tag{1}$$

where α_0 and β_0 are the mean *P* and *S* velocities of the medium. We assume that the fractional density fluctuations are proportional to the velocity variations (S&F equation 4.48):

$$\frac{\Delta\rho(\mathbf{x})}{\rho_0} = \nu\xi(\mathbf{x}), \tag{2}$$

where ν is the density/velocity fluctuation scaling factor. Obtaining a reliable estimate for ν in the mantle is difficult. Analysis of long-wavelength *P* and *S* velocity anomalies in mantle tomography models has led to ν estimates of approximately 0.7 (Masters, private communication, 2004), but these estimates assume a thermal origin for the velocity perturbations, whereas the small-scale anomalies relevant to the high-frequency scattering problem are almost certainly compositional (Hedlin *et al.* 1997). Examples presented in this paper will use $\nu = 0.8$, an estimate for the lithosphere obtained using Birch's Law (S&F p. 101). Larger values of ν will generally increase the amount of backward scattering.

The basic scattering patterns are given by (S&F equation 4.50):

$$\begin{aligned}
X_r^{PP}(\psi,\zeta) &= \frac{1}{\gamma_0^2}\left[\nu\left(-1+\cos\psi+\frac{2}{\gamma_0^2}\sin^2\psi\right)-2+\frac{4}{\gamma_0^2}\sin^2\psi\right],\\
X_\psi^{PS}(\psi,\zeta) &= -\sin\psi\left[\nu\left(1-\frac{2}{\gamma_0}\cos\psi\right)-\frac{4}{\gamma_0}\cos\psi\right],\\
X_r^{SP}(\psi,\zeta) &= \frac{1}{\gamma_0^2}\sin\psi\cos\zeta\left[\nu\left(1-\frac{2}{\gamma_0}\cos\psi\right)-\frac{4}{\gamma_0}\cos\psi\right],\\
X_\psi^{SS}(\psi,\zeta) &= \cos\zeta\,[\nu(\cos\psi-\cos 2\psi)-2\cos 2\psi],\\
X_\zeta^{SS}(\psi,\zeta) &= \sin\zeta\,[\nu(\cos\psi-1)+2\cos\psi],
\end{aligned} \tag{3}$$

where X_r^{PP} is the radial component of *P*-to-*P* scattering, $X\psi^{PS}$ is the ψ component of *P*-to-*S* scattering, etc. The angles ψ and ζ are defined as in Fig. 5 and the velocity ratio $\gamma_0 = \alpha_0/\beta_0$. In general, γ_0 varies somewhat in the Earth, particularly in the inner core

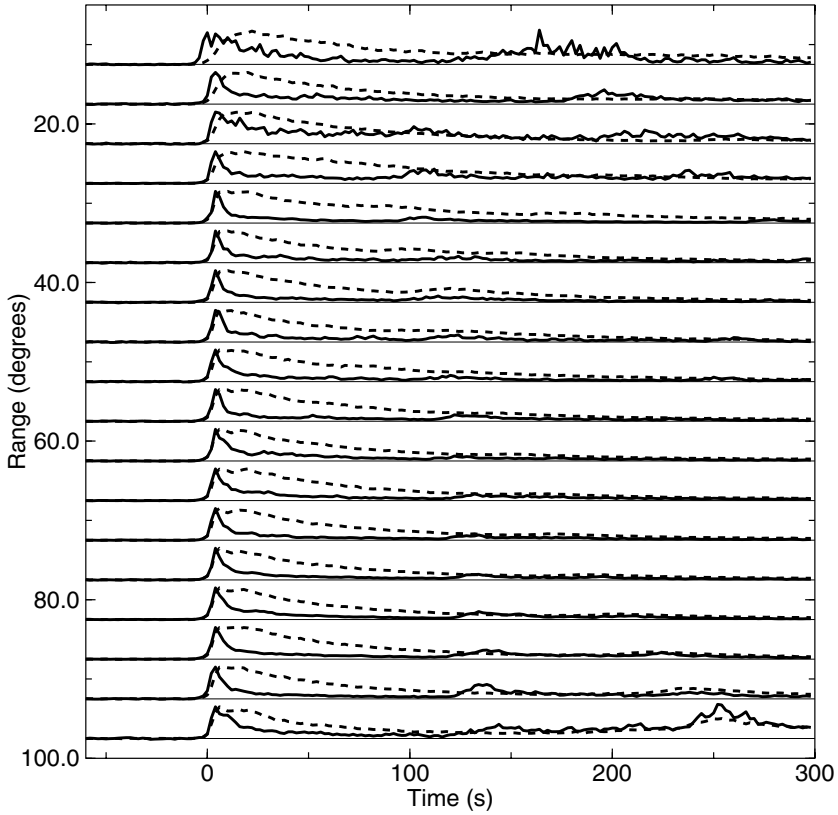

Figure 4. A comparison between the shallow-event, envelope-function stack (dashed line) and the deep-event stack (solid line). Time is relative to *P* and the stacks have been scaled to the same *P*-wave maximum amplitude. Note the much more extended coda from the shallow events.

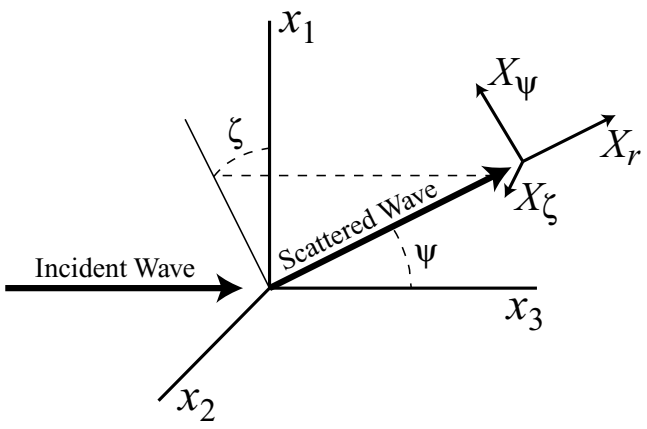

Figure 5. The ray-centred coordinate system used in the scattering equations. The incident ray is in the x_3 direction. For *S* waves the initial polarization is in the x_1 direction. The scattered ray direction is defined by the angles ψ and ζ. The scattered ray polarization is defined by X_r, X_ψ and X_ζ.

where the *S* velocity is anomalously small. Here we are concerned with crust and mantle scattering and approximate γ_0 to a constant value given by the average for the PREM model within the scattering layer. For most of the mantle, the γ_0 values are between 1.8 and 1.9.

Assuming a random media model, the scattered power per unit volume is given by the scattering coefficients for the various types of scattering (*P* to *P*, *P* to *S*, etc.; S&F equation 4.52):

$$
\begin{aligned}
g^{PP}(\psi,\zeta;\omega) &= \frac{l^4}{4\pi}\left|X_r^{PP}(\psi,\zeta)\right|^2 P\left(\frac{2l}{\gamma_0}\sin\frac{\psi}{2}\right),\\
g^{PS}(\psi,\zeta;\omega) &= \frac{1}{\gamma_0}\frac{l^4}{4\pi}\left|X_\psi^{PS}(\psi,\zeta)\right|^2\\
&\quad P\left(\frac{l}{\gamma_0}\sqrt{1+\gamma_0^2-2\gamma_0\cos\psi}\right),\\
g^{SP}(\psi,\zeta;\omega) &= \gamma_0\frac{l^4}{4\pi}\left|X_r^{SP}(\psi,\zeta)\right|^2\\
&\quad P\left(\frac{l}{\gamma_0}\sqrt{1+\gamma_0^2-2\gamma_0\cos\psi}\right),\\
g^{SS}(\psi,\zeta;\omega) &= \frac{l^4}{4\pi}\left(\left|X_\psi^{SS}(\psi,\zeta)\right|^2+\left|X_\zeta^{SS}(\psi,\zeta)\right|^2\right)\\
&\quad P\left(2l\sin\frac{\psi}{2}\right),
\end{aligned}
\tag{4}
$$

where $l = \omega/\beta_0$ is the *S* wavenumber for angular frequency ω, *P* is the power spectral density function (PDSF) for the random media model (see S&F p. 14–17). For a model characterized by an exponential autocorrelation function we have (S&F equation 2.10):

$$
P(m) = \frac{8\pi\epsilon^2 a^3}{(1+a^2m^2)^2}, \tag{5}
$$

where a is the correlation distance, ϵ is the rms fractional fluctuation [$\epsilon^2 = \langle\xi(\mathbf{x})^2\rangle$] and m is the wavenumber. We assume an exponential autocorrelation function for the modelling results presented in this paper; if desired other PDSF models could easily be implemented by substituting the appropriate equation for $P(m)$.

The total scattering coefficients g_0^{PP}, etc., are given by the averages of these coefficients over the unit sphere. The mean free path ℓ for

a ray between scattering events is given by the reciprocals of these coefficients:

$$\ell^P = \frac{1}{g_0^{PP} + g_0^{PS}}$$
$$\ell^S = \frac{1}{g_0^{SP} + g_0^{SS}}. \quad (6)$$

3.1 Computational specifics

The calculations are performed for a constant angular frequency ω. We assume that the properties of each distinct scattering region can be approximated with fixed values of the rms fluctuation ϵ, correlation length a, S wavenumber l, density/velocity scaling parameter ν and P/S velocity ratio γ_0. We then pre-compute values for g over 1.8° increments in the scattering angles ψ and ζ. These values are stored and used both to numerically average the g functions over the unit sphere to determine g_0 and later as weights in order to compute random scattering angles with the correct probabilities. We found a 1.8° spacing to be adequate for the calculations in this paper. Finer spacing could be used for greater accuracy in the case of very low angle scattering (this would not significantly increase the computation time for the random rays, provided sufficient computer memory is available). The polarization of scattered S waves is determined by the relative size of the X_ψ and X_ζ terms. Thus, we compute and store the scattered S-wave polarizations at the same time that we pre-compute the g values.

3.2 Whole-space results

To test our approach, we first compute results for a whole-space model with uniform scattering properties and no intrinsic attenuation. In this case, ray paths between scattering points are straight lines. P and S phonons are sprayed from the source in a specified direction. We permit different initial energies E_i^P and E_i^S for P and S waves. Because theoretical results show that a double-couple source, averaged over all directions, will radiate in total 23.4 times more S energy than P energy (e.g. Sato 1984, eq. 50e), we set $E_i^S = 23.4\ E_i^P$. Of course this would not apply to individual phonons radiated from a double-couple source, but because in this example we are interested only in the average response over all takeoff angles (or, equivalently, at fixed receiver point the average over random orientations of the double-couple source), we can apply the average result to the individual phonons.

For each phonon, the probability of scattering is constant along its ray path, so the path length r to a scattering event is given by an exponentially distributed random number with mean value ℓ^P or ℓ^S for P waves and S waves, respectively. Thus individual values of r are computed as

$$r_P = -\ell^P \ln x,$$
$$r_S = -\ell^S \ln x, \quad (7)$$

where x is a random number between 0 and 1. When a scattering event occurs, a second random number is used to decide whether the scattered wave is P or S, according to the relative sizes of g_0^{PP} and g_0^{PS} for an incident P wave or g_0^{SP} and g_0^{SS} for an incident S wave. A third random number is then used to determine the scattering angle (ψ and ζ) and the S polarization (if required) using the stored array containing the g values as a function of ray angle. The range of permitted scattering angles is determined by how finely this array samples ψ and ζ. The phonon then travels along its new ray direction until the next scattering event. The calculation for each phonon continues until a maximum time limit is reached, at which point the algorithm starts over with a new phonon from the source.

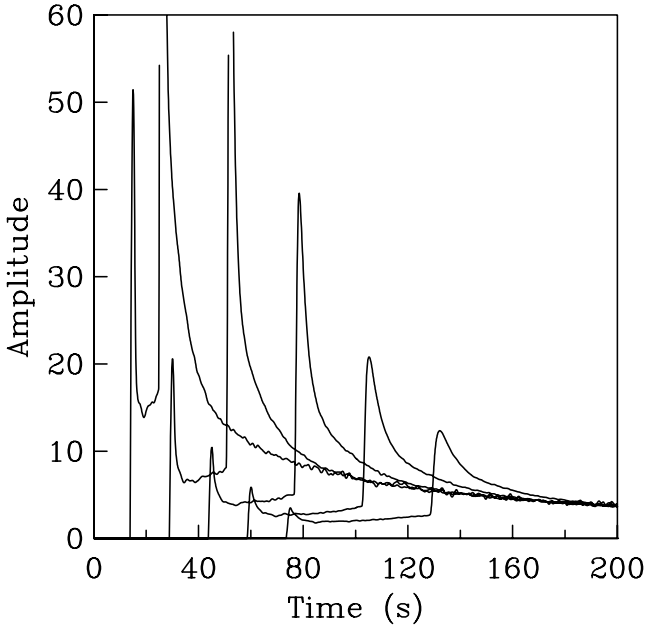

Figure 6. Synthetic envelope functions computed using the seismic phonon method for an isotropic source within a whole-space of uniform average velocity of 6.7 km s $^{-1}$. Results are plotted for receivers at 100 to 500 km. The S-wave peaks for the 100 and 200 km receiver extend off the top of the plot. Note the convergence of the S-wave codas at large times. See text for details of the material properties.

In our whole-space calculation, we compute the average energy arriving at a set of specified distances from the source as a function of time. A time-series with digitization interval dt is defined for each distance. For each ray segment, we check to see if the ray intersects any of the spheres around the source defined by these distances. In general, there will be be zero, one, or two intersection points. For each intersection point, we add E_i to the appropriate time-series at the nearest point to the computed intersection time.

The results plotted in this section were computed for $\omega = 2\pi$ (i.e. 1 Hz), $\alpha_0 = 6.7\,\mathrm{km\,s^{-1}}$, $\gamma_0 = \sqrt{3}$, $\nu = 0.8$, $\epsilon = 0.05$, $a = 2$ km, $dt = 0.1$ s and receiver radii of 100 to 1000 km. This yields mean free paths of 137 km for P waves and 55 km for S waves. Fig. 6 plots amplitude versus time for receivers at 100 to 500 km. Notice that the amplitudes of the direct P and S arrivals decay with range from the source, but that at large times all of the S coda amplitudes converge to the same value. This is consistent with the results of Frankel & Wennerberg (1987) that indicate coda energy eventually becomes spatially uniform in a region well behind the advancing S wave front. One might also expect that ray directions and S-wave polarizations will become randomized after a significant number of scattering occurrences. This is confirmed by Fig. 7, which plots ray directions and polarizations for S waves, using 500 initial rays, after 1, 5 and 20 scattering events (these events may include S-to-P and P-to-S scattering provided the final wave is S). Traces of the original polarization can be seen even after 10 scattering events, but the ray is essentially completely randomized after 20 scattering events.

For multiple scattering, theory predicts that the time dependence of energy density should converge asymptotically to the diffusion solution, given by a $t^{-1.5}$ decay rate (e.g. Zheng 1991; S&F p. 180). This is shown for our simple whole-space model in Fig. 8, which plots power versus time at 500 km range as compared to the $t^{-1.5}$

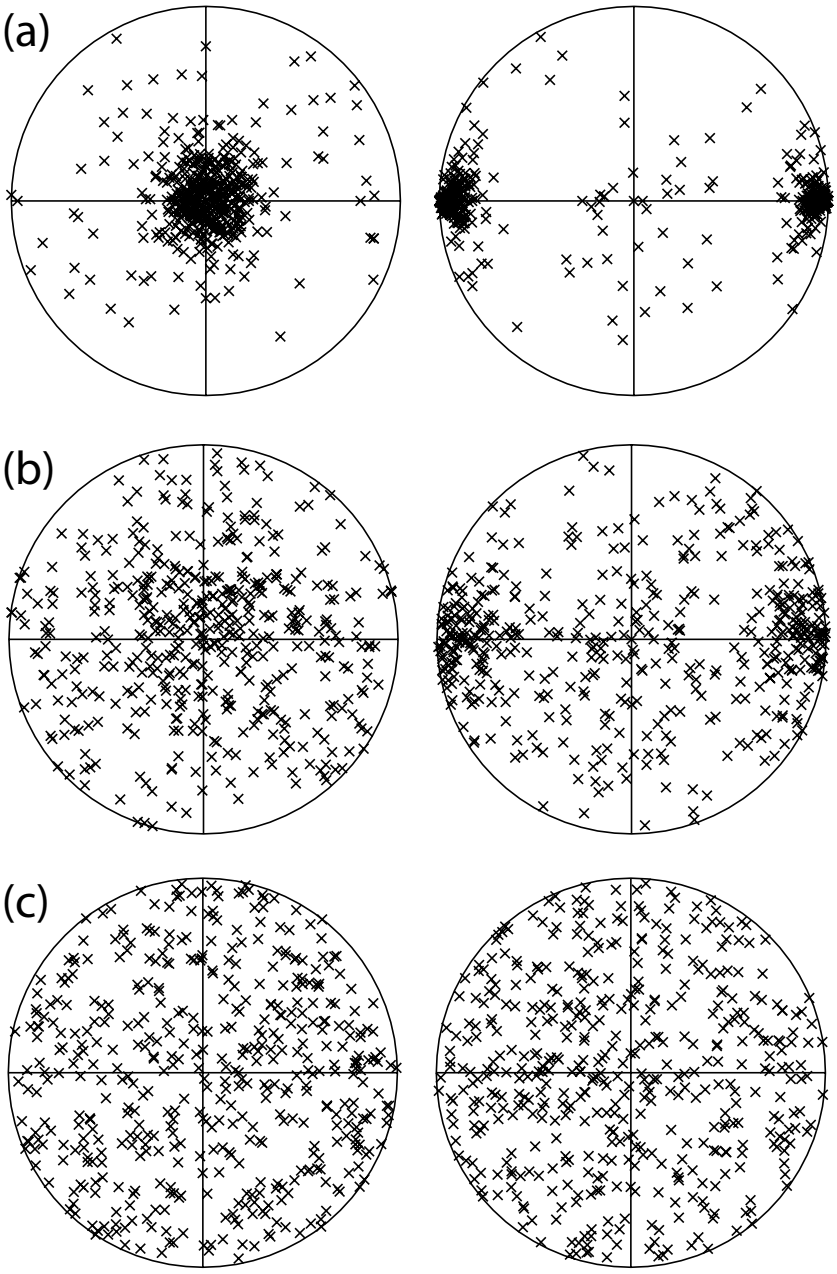

Figure 7. Examples of ray directions (left) and *S*-wave polarizations (right) for the whole-space test of the seismic phonon method. Results are shown for 500 rays following (a) a single scattering event, (b) 10 scattering events and (c) 20 scattering events. An equal area projection is used with the outer circle representing angles 90° away from the centre. The initial ray direction is at the centre of the plots; the initial *S* polarization is at the left and right edges of the plots, perpendicular to the ray direction. Note the gradual randomization of the directions and polarizations after increasing numbers of scattering events.

line predicted on the log–log plot. A final theoretical check on our method is provided by the ratio of *P*-wave energy density to *S*-wave energy density, which should asymptotically approach $1/2\ \gamma_0^3$ ($= 0.096$ for $\gamma_0 = \sqrt{3}$) at large lapse times (S&F p. 222). This ratio is plotted in Fig. 9 for the whole-space model with a receiver at 1000 km range from the source. Note that to correctly obtain energy density, the energy of each arriving phonon is divided by the wave velocity.

4 APPLICATION TO GLOBAL MODELS

Although the principles of the phonon approach are quite simple, efficient implementation of the method on the computer for realistic global Earth models requires a number of additional considerations. Here we describe in greater detail how our complete algorithm works.

(i) We use the IASP91 Earth model but slightly smooth the sharp corner in the velocity profile at 2740 km depth to avoid an abrupt change in ray theoretical amplitudes near 90° caused by the reduced velocity gradient within the D″ layer.

(ii) To avoid repeatedly calculating ray paths, we first compute *dx* and *dt* values within 10-km-thick layers in the model for 10 000 values of ray parameter ranging from zero to the slowest velocities in the model. We save these results in separate arrays for *P* and *S* waves. The starting phonons that are sprayed from the source are restricted

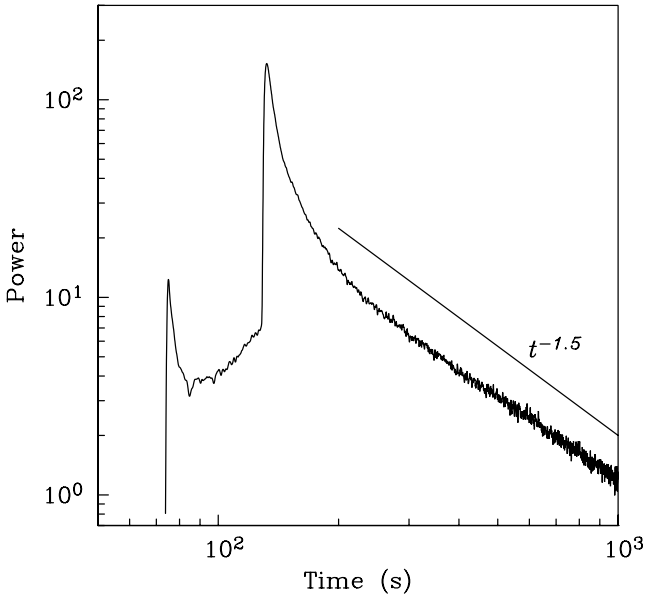

Figure 8. Power versus time for the whole-space test of the seismic phonon method at 500 km range, showing the expected $t^{-1.5}$ falloff at large times.

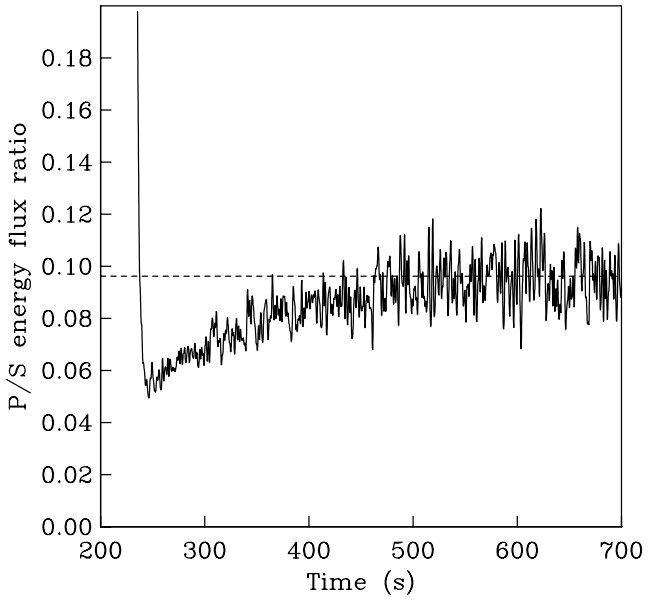

Figure 9. The *P*-to-*S* energy density ratio as a function of time for the whole-space test of the seismic phonon method at 1000 km range. Note the approximate convergence to the theoretically expected value (dashed line).

to these ray parameters. In general, equal sampling in ray parameter yields more phonons with small ray parameters than a spherically symmetric source would produce. Thus, the initial energy assigned to each phonon is adjusted to account for this, using geometrical spreading considerations for an isotropic source.

(iii) *S*-wave polarization is specified for each phonon as an angle within an *SV*/*SH* coordinate system. Note that these angles will typically change following a reflection, transmission, or scattering event. Initial *S* polarizations from the source are randomly assigned.

(iv) Intrinsic attenuation is included by specifying values for *P*-wave attenuation Q_α within fixed depth intervals. For simplicity, corresponding values for *S*-wave attenuation are obtained from $Q_\beta = (4/9)\, Q_\alpha$, an approximation that assumes a Poisson solid and that all attenuation is in shear. It would not be difficult to separately input Q_β but this level of detail is not necessary in our first-order analysis. The effect of Q is modelled by accumulating a value of $t^* = \int dt/Q$ for each phonon along its path. When the phonon strikes the surface, the energy contribution is proportional to $e^{-\omega t*}$. We used the Warren & Shearer (2000) mantle attenuation model as a starting point for most of our global models because it is obtained from short-period *P* waves similar to those in our data stacks. This model is frequency-dependent; at 1 Hz, $Q_\alpha = 227$ from 0 to 220 km and $Q_\alpha = 1383$ from 220 to 2889 km. However, we found that better fits to our coda observations could be achieved by using higher values of Q_α (i.e. less attenuation). This is not unexpected because the Warren & Shearer model, derived from spectral falloff in 0.16 to 0.86 Hz *P* waves, likely includes both scattering and intrinsic attenuation.

(v) At model interfaces, energy-normalized *P*/*SV* and *SH* reflection and transmission coefficients are pre-computed for all values of ray parameter. When an individual phonon strikes an interface, the energy within the phonon is not partitioned into different parts for the scattered waves. Rather, these coefficients are translated into probabilities that are used to randomly pick the wave type and direction for a single phonon that leaves the interface. In this way, the energy partitioning at interfaces is modelled stochastically as the average response of thousands of individual phonons. This greatly simplifies the code because it needs to track only a single phonon at a time, not multiple phonons generated at each interface. By shooting millions of rays through the model, it is possible to generate all possible ray paths automatically without the need to specify each one. Note that some care must be taken to correctly assign these probabilities in the case of an incident *S* wave of arbitrary polarization. In this case, the probability of a conversion to *P* increases as the ratio of *SV* to *SH* energy increases. The polarization of a scattered *S* phonon depends both on the incident polarization and on the *SV* and *SH* coefficients. Calculations in this paper assumed four interfaces: the surface, the Moho, the CMB and the inner-core boundary (ICB; except for the examples in Section 4.1, which do not include the Moho).

(vi) The source is arbitrarily assigned to the equator at zero longitude and the phonon takeoff azimuth to 90°. A fixed initial azimuth can be used owing to the isotropic source assumption and the fact that results are eventually summed over all azimuths. Phonon locations are specified in three-dimensions (latitude, longitude and depth). When a phonon strikes the surface, the distance to the source location is computed and the energy contribution is added to the appropriate distance–time bin. Using the ray angle and polarization, separate contributions to the vertical-, radial- and transverse-component wavefield may be computed for later comparison to three-component seismic data. We use 0.5° distance bins and 1-s time bins. The surface energy density is computed by normalizing by the area within each distance bin (representing a ring surrounding the source).

(vii) Scattering regions are specified as layers with fixed values of the rms fluctuation ϵ, correlation length a, *S* wavenumber l, density/velocity scaling parameter ν and *P*/*S* velocity ratio γ_0. In general, $l = \omega/\beta_0$ varies with depth in the Earth. However at the level of detail considered in our modelling, we found that results using a fixed value of l over 1000-km-thick layers were not significantly different from those obtained using a finer layer spacing. As in the whole-space calculation discussed above, we pre-compute values of the scattering coefficients g and use these to assign scattering probabilities. When a phonon first enters a scattering layer, a path length to a scattering event is randomly assigned (see eq. 7). If the phonon

is still within the scattering layer after travelling this distance, then a scattering event occurs. The scattered wave will have a new azimuth and takeoff angle, which may be either upward or downward.

4.1 Examples with no scattering

As a test of our seismic phonon method, we first computed results for models with no scattering. In this case, the phonons should all arrive along the traveltime curves for known seismic phases. A somewhat contrived illustration of this is provided by Fig. 10, which plots the wavefield image (total energy on all three components) resulting from a model with no attenuation and which forces the reflection and transmission coefficients at the model interfaces to have equal values. In this case, an individual phonon striking an interface will have an equal chance of converting into each of the possible scattered waves. The result is the automatic generation of all possible ray theoretical traveltime curves that the model can produce, regardless of their actual amplitudes. This plot may be useful in some situations to compare to an observed arrival to see if it corresponds to the time of any theoretical arrivals.

A more realistic image of the predicted global wavefield is shown in Fig. 11, which plots the vertical-component wavefield produced using the actual reflection and transmission coefficients and the Warren & Shearer (2000) mantle attenuation model ($Q_\alpha = 227$ from 0 to 220 km, $Q_\alpha = 1383$ from 220 to 2889 km) and the Bhattacharyya *et al.* (1993) inner core attenuation model ($Q_\alpha = 360$). In this case, most of the traveltime curves shown in Fig. 10 disappear, owing to their predicted low amplitudes. In particular, attenuation eliminates most *S*-wave arrivals at 1-Hz frequency. For comparison to these synthetics, Fig. 12 shows an image of the observed global high-frequency vertical component, obtained using a stacking method the emphasizes first arrivals (Astiz *et al.* 1996). In general, there is good agreement regarding the relative visibility of the different seismic phases.

5 MODELLING GLOBAL *P* CODA OBSERVATIONS

We now describe our use of the phonon method to model the global *P* coda stacks described earlier and presented in Figs 1 to 4. This involves attempting to match both the shape of the individual coda envelopes and the range dependence of the amplitudes. Although some modelling of coda envelopes and teleseismic *P* coda has previously been performed (e.g. Korn 1990; Sato 1991; Wagner & Langston 1992; Korn 1993, 1997), to our knowledge this is the first

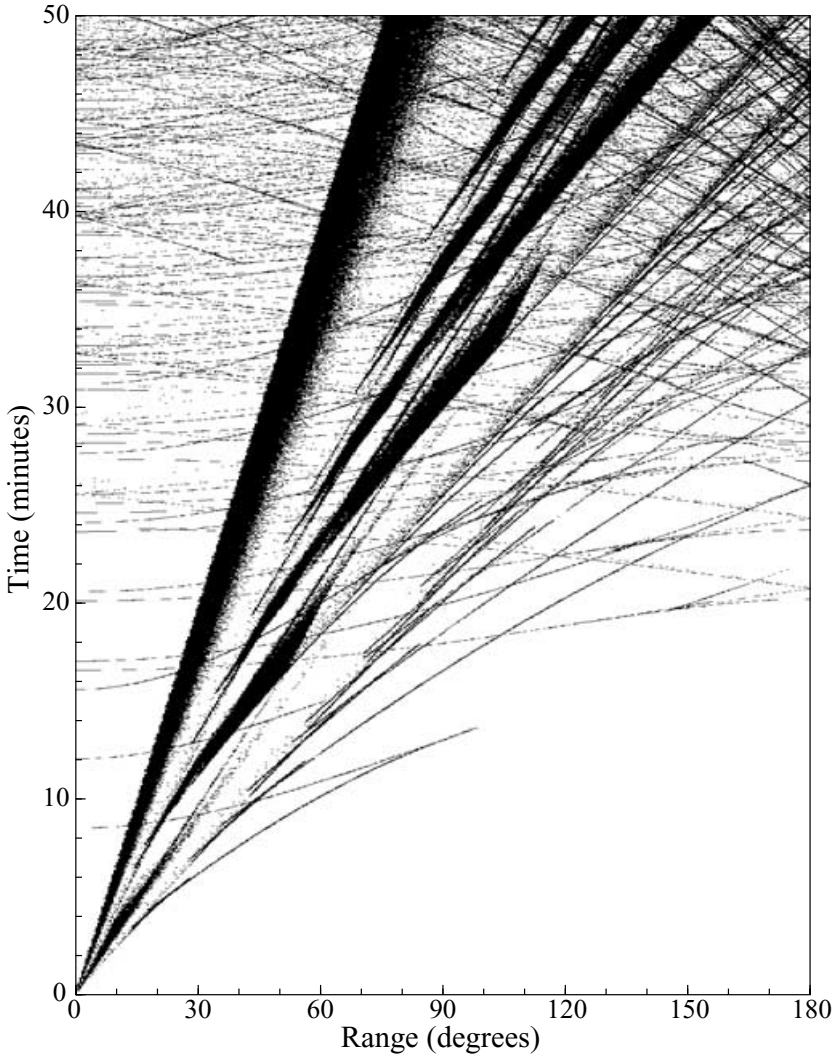

Figure 10. Theoretical traveltime curves predicted using the seismic phonon method. Most of these have amplitudes too small to see in real data.

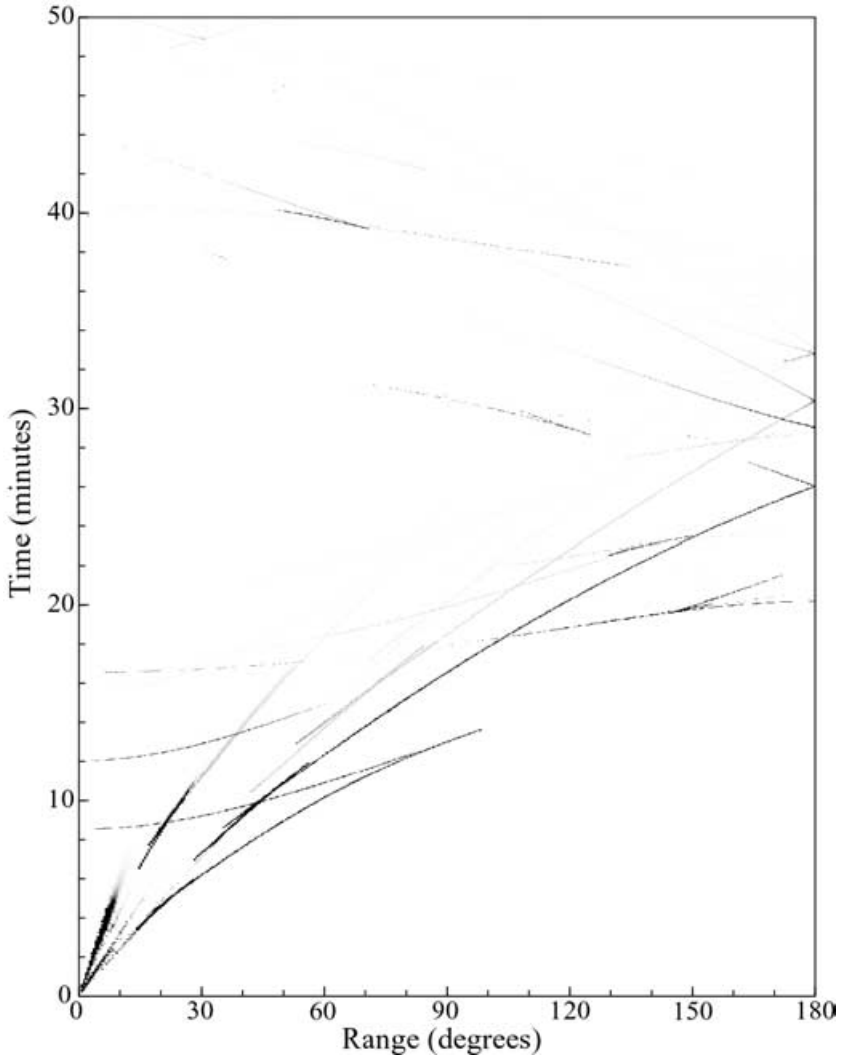

Figure 11. Predicted amplitudes for the 1-Hz, vertical-component wavefield computed using the seismic phonon method, assuming a realistic attenuation model.

attempt to explain the globally averaged time and distance properties of *P* coda with a self-consistent model that accounts for scattering at all depths in the Earth. We wish to emphasize, however, that our results are applicable only at the ∼1-Hz band of our data stacks and that we consider only relative amplitudes, not absolute amplitudes.

So far, because of limitations in our available computer power, our analysis has been restricted to forward modelling rather than any kind of formal inversion. The method is readily suited to parallel computations, which would permit much more detailed exploration of the model parameter space in future studies. We have attempted here only to test whether fairly simple first-order models exist that can provide a reasonable fit to the data. Although slightly better fits can be obtained by separate modelling of the shallow- and deep-event stacks, we found that a reasonable overall fit to both data sets could be obtained with a single model. This model has scale length $a = 4$ km and rms perturbation $\epsilon = 0.04$ between 0 and 200 km, $a = 4$ km and $\epsilon = 0.03$ between 200 and 600 km, $a = 8$ km and $\epsilon = 0.005$ between 600 km and the CMB, velocity versus density scaling parameter $\nu = 0.8$, and intrinsic attenuation $Q_\alpha = 450$ between 0 and 200 km and $Q_\alpha = 2500$ between 200 km and the CMB. This yields mean free paths of $\ell^P \sim 140$ km and $\ell^S \sim 50$ km in the upper 200 km, $\ell^P \sim 300$ km and $\ell^S \sim 100$ km between 200 and 600 km, and $\ell^P \sim 10\,000$ km and $\ell^S \sim 3300$ km in the lower mantle (the exact values are depth-dependent).

We explicitly include the effect of discontinuities at the surface, Moho, CMB and ICB, but not reflected and converted phases from the upper-mantle discontinuities (the addition of the 410 and 660 km discontinuities has only a very minor effect on coda amplitudes). Of course, the traveltime triplications associated with the velocity increases at these discontinuities are included in the modelling. We generate equal numbers of radiated *P* and *S* phonons, with the *S* phonons 23.4 times more energetic. The source is assumed to be isotropic with both upgoing and downgoing takeoff angles included. Initial *S* polarizations are randomly assigned.

5.1 Deep-event modelling

We model the deep events using only a single source depth at 600 km, even though the data stack includes events varying in depth between 400 and 700 km. In principle, this difference should cause the *PP* image to be broader in the data than in the synthetics, but in practice we did not notice a significant problem in the fit to *PP*. Fig. 13 shows the fit of the vertical amplitude of our synthetics (computed for 49 million phonons) to the data stack, plotting separately (a) the

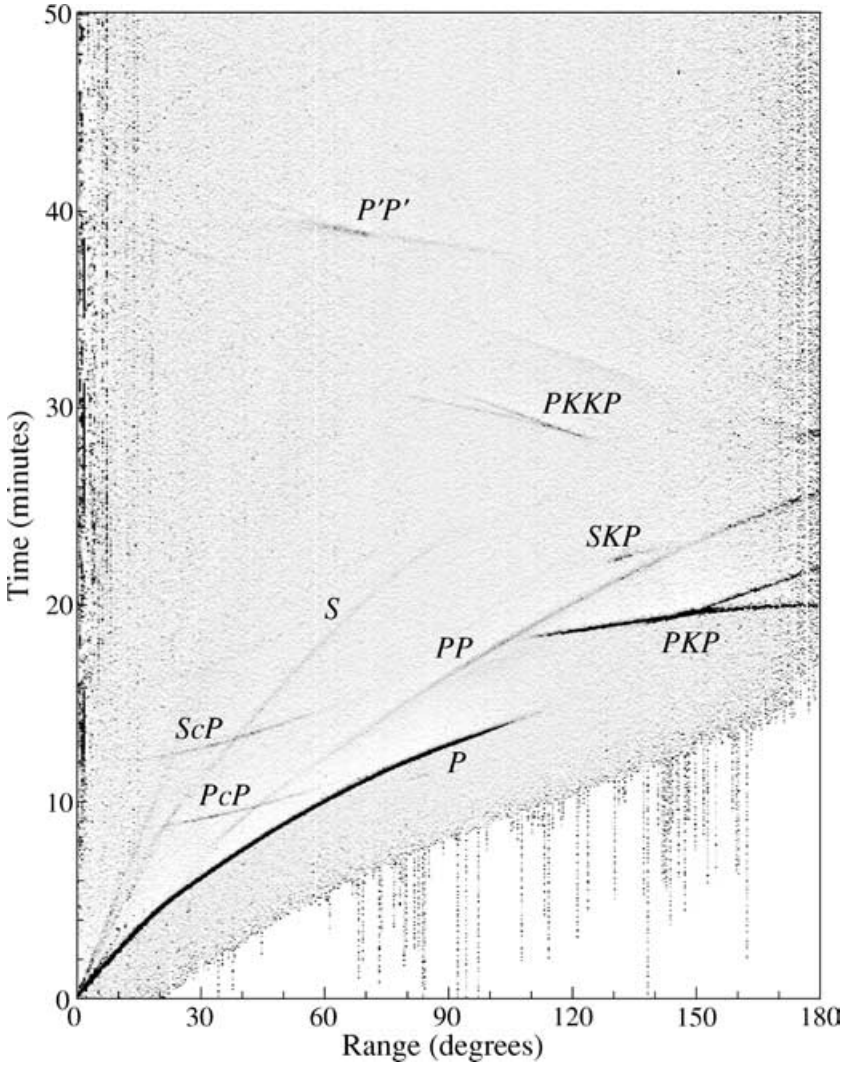

Figure 12. Observed high-frequency (0.5 to 2 Hz), vertical-component wavefield obtained using a short-term-average to long-term-average stacking method by Astiz *et al.* (1996). The onset of the speckling several minutes before the *P* arrival is an artefact as a result of the limited time windows of the seismograms used in the stack.

peak amplitude versus distance and (b) the shape of the *P* coda envelopes.

The synthetic amplitudes fit reasonably well between approximately 30° and 95° range, but the model predicted amplitudes are too high at shorter and longer ranges and do not contain the broad amplitude peak seen in the data between 45° and 65°. We are not sure what is causing the amplitude misfit between 10° and 30° but did not emphasize this distance range in our modelling because it is susceptible to *P* amplitude variations caused by differences in upper-mantle velocity gradients. The falloff in the data amplitudes beyond 95° is likely caused by finite frequency effects related to the influence of the core; ray theoretical methods like ours do not correctly predict *P* amplitudes for rays turning near the CMB. The synthetic amplitudes decrease steadily between 30° and 80° but the data amplitudes contain a bulge near 50°. The slope of the amplitude falloff in the synthetics can be adjusted by changing intrinsic *Q* in the model, but we were not able to find any models that predict the amplitude bulge seen in the data. We suspect that this feature may be an artefact of the uneven distribution of sources for the deep events, which are dominated by the Tonga region, and thus may not represent an unbiased global average.

Fig. 13(b) shows the fit to the *P* coda, after normalizing to equal energies in the first 30 s and aligning on the theoretical *P* arrival time. Some numerical noise is apparent in the synthetic coda; this is an artefact of the limited number of phonons used in our calculation. *P* coda and *PP* (the small bump at approximately 120 s) are well fit between approximately 30° and 85°. *PP* is hard to see in this plot except beyond approximately 85° (it is the large bump in the 95° –100° data stack at approximately 250 s), where it is underpredicted by the synthetics. This misfit is likely caused by overprediction of the direct *P* amplitude in our ray theoretical calculations (see previous paragraph). The predicted coda envelopes generally slightly underpredict the peak amplitude and overpredict the coda amplitude at approximately 20 s after the *P* arrival. At ranges less than 30°, the synthetics underpredict *PP* amplitudes and have *S* envelopes that are approximately the right shape and amplitude but that arrive too early.

5.2 Shallow-event modelling

We model the shallow-event data stack with a single source at 20 km depth (including both upgoing and downgoing rays), rather than the

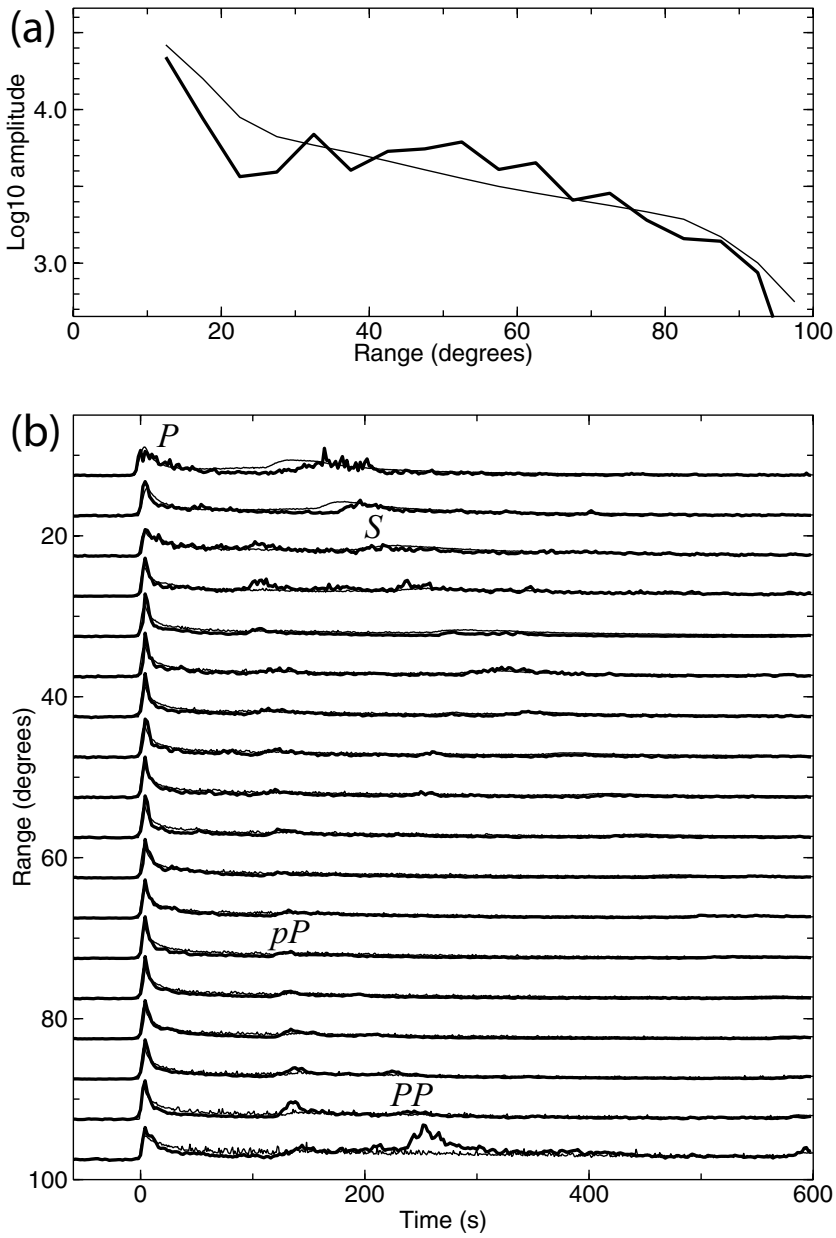

Figure 13. Comparisons between the envelope stack for deep-event data (heavy line) with the predictions of the phonon method applied to a scattering model (thin line). (a) Peak *P*-wave amplitude as a function of source–receiver distance. (b) Coda envelopes in 5° range bins plotted as a function of time from the direct *P* arrival. Amplitudes are normalized to the same energy in the first 30 s. See text for a description of the deep-source scattering model.

specific range of source depths (up to 50 km) included in the data stack. As in the case of the deep-event modelling, this does not appear to limit our ability to fit the data. Fig. 14 shows the fit of the vertical amplitude of our shallow-event synthetics (computed for 42 million rays) to the data stacks. The overall fit of our model predictions to *P* amplitude and *P* coda shape is fairly good. We overpredict *S* amplitudes at short ranges and underpredict *PP* amplitude between 95° and 100°, but, as discussed above, we expect our method to be most accurate between approximately 30° and 80°. The amplitude decay with distance between 25° and 85° is well matched by the synthetics and provides one of the primary constraints on intrinsic attenuation (Q_α) in the lower mantle.

As in the case of the deep-event modelling, observed *PP* amplitudes near 100° are not matched in the synthetics. The model slightly under predicts *P* coda levels between 50 and 100 s near 25° and over predicts *S* amplitudes between 10° and 30°. The fit to the *S* amplitudes can be improved by increasing Q_α in the uppermost mantle or by reducing the amount of *S* energy radiated by the source, but this worsens the fit to the *P* coda at short distances by reducing the predicted coda amplitude. In general, our model represents a compromise between fitting different individual features in the data stacks.

5.3 Discussion

The overall fit of our model predictions to *P* amplitude, *P* coda shape and *PP* amplitude is fairly good between approximately 30° and 90° range, where we might expect the teleseismic wavefield to be reasonably well behaved and suited to modelling with ray theoretical methods such as our phonon algorithm. However, we

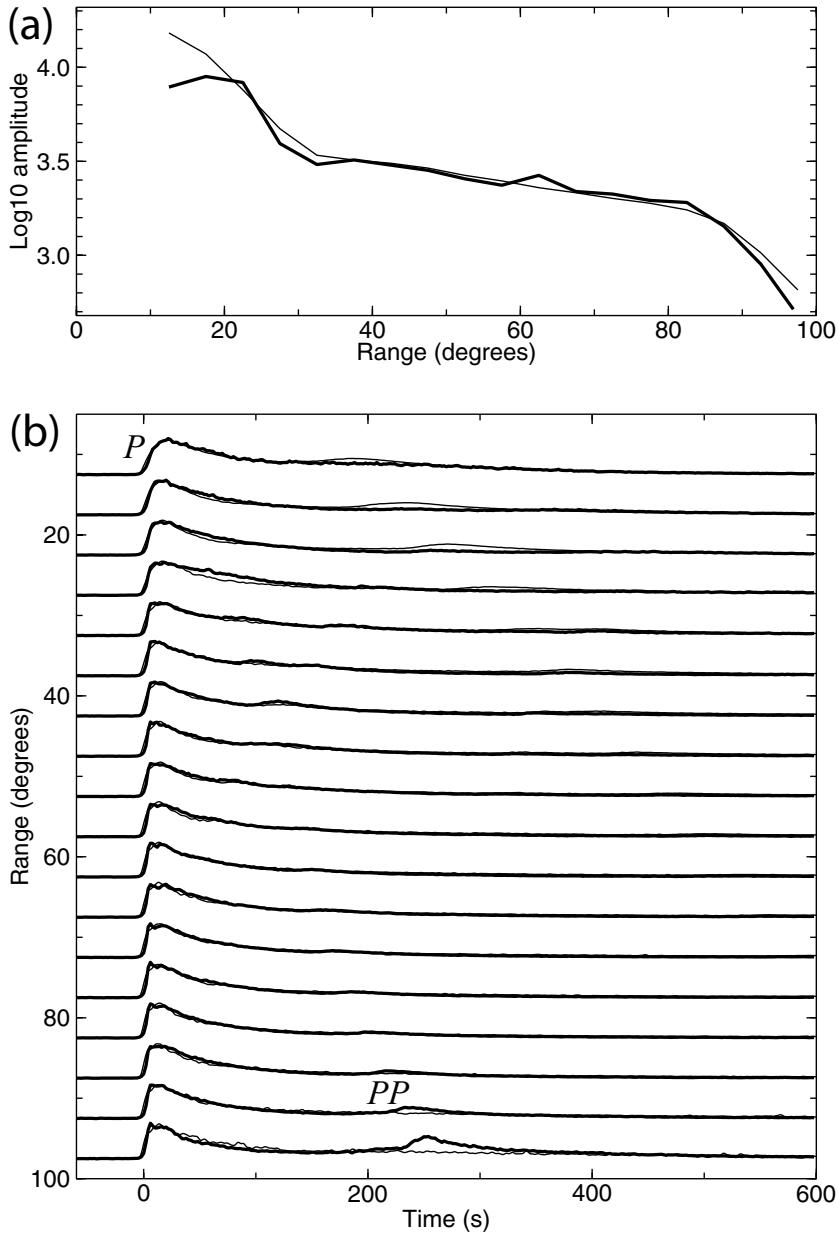

Figure 14. Comparisons between the envelope stack for shallow-event data (heavy line) with the predictions of the phonon method applied to a scattering model (thin line). (a) Peak *P*-wave amplitude as a function of source–receiver distance. (b) Coda envelopes in 5° range bins plotted as a function of time from the direct *P* arrival. Amplitudes are normalized to the same energy in the first 30 s. See text for a description of the shallow-source scattering model.

have not explored enough different models to place any kind of realistic uncertainties on the various model parameters. Certainly there is a trade-off between the thickness of the upper-mantle layer in our model and its scattering strength (i.e. thinner layers with stronger scattering would also work) and models with more layers would also be possible. Because our upper-mantle layer is much more heterogeneous than the lower-mantle layer, our model is consistent with previous results that suggest that scattering is much stronger near the surface than deeper in the mantle.

There is also a trade-off between the correlation distance a in our exponential autocorrelation model and the rms fluctuation ϵ. In general, smaller values of a require larger values of ϵ. For example, fits approximately as good as those plotted in Figs 13 and 14 are obtained for lower-mantle values of $a = 4$ km, $\epsilon = 0.007$ and $a = 16$ km, $\epsilon = 0.0035$, and for upper-mantle values of $a = 2$ km, $\epsilon = 0.055$ for 0 to 200 km and $a = 2$ km, $\epsilon = 0.04$ for 200 to 600 km. However, it is not possible to fit both the shallow- and deep-event data stacks with models in which the correlation length is significantly longer than 4 km in the upper mantle. For example, models with $a = 8$ km in the upper mantle either predict too little shallow-event coda or too much deep-event coda. Because the scattering angles become larger at small values of a, the implication is that relatively wide angle scattering is required in the crust and uppermost mantle.

Resolving the trade-off between correlation distance and rms fluctuation in more detail will require examining results at different frequency bands: we do not attempt such an analysis here and highlight the $a = 8$ km result for the lower mantle only because it is comparable to the wavelength of the 1-Hz mantle *P* waves that are

the focus of this study. There is also a trade-off between scattering strength and intrinsic attenuation (Q_α), at least in terms of fitting the *P* amplitude decay with distance. As discussed above, some constraint on Q_α is provided by the limited amplitude of *S* in the data stacks. If the model contains too little crust and upper-mantle intrinsic attenuation, the amplitude of *S* in the synthetics becomes very large.

An important question is whether we can truly resolve that nonzero scattering is occurring in the lower mantle, as recent studies have indicated. Our modelling suggests some lower-mantle scattering because models without lower-mantle scattering tend to underpredict *P* coda amplitudes at distances beyond approximately 50°. We fit both the shallow and deep data stacks with an rms velocity perturbation of 0.5 per cent in the lower mantle, not too far from the 1.0 per cent value obtained from *PKP* precursors by Hedlin *et al.* (1997) but significantly more than the value of 0.1 to 0.2 per cent obtained by Margerin & Nolet (2003b) for *PKP* precursors. Our predicted *S*-wave mean free path of ∼3300 km in the lower mantle is roughly comparable to estimates obtained by Lee *et al.* (2003) from radiative transfer modelling of *ScS* coda. Comparisons between studies should be made with some caution, however, because of differences in modelling assumptions. Lee *et al.* (2003) assume isotropic scattering and the Margerin & Nolet (2003b) values are for a different model of the heterogeneity spectrum than the $a =$ 8 km exponential model that we use. Resolving lower-mantle scattering models is an important goal for future research because of the implications that small-scale perturbations have on compositional heterogeneity in the mantle.

Our modelling suggests stronger scattering in the lithosphere and upper mantle than in the lower mantle. Previous studies of lithospheric scattering from regional measurements, as summarized by S&F suggest *S*-wave mean free paths of 25 to 250 km, compared with our predicted *S*-wave mean free path of 50 km within the uppermost 200 km of our model. It is worth noting that most of the previous analyses have assumed isotropic scattering, whereas our model involves more directional scattering events. The *S*-wave momentum transfer mean free path (e.g. Gusev & Abubakirov 1996; Saito *et al.* 2003) for our model is approximately 900 km in the uppermost 200 km.

Our modelling approach includes many aspects of global scattering, including both *P* and *S* waves, intrinsic attenuation and depth-dependent properties. We have identified a fairly simple model that explains the main features seen in high-frequency *P* amplitudes and *P* coda for globally averaged stacks of both shallow and deep events. However, there are other factors that may be important that we have not considered in any detail, including those that follow below.

(i) Lateral variations in scattering strength could be significant. In particular, our results could be biased if scattering is stronger than the global average in shallow-earthquake source regions. This would break the assumed symmetry between the amount of scattering expected at shallow depths near the source and that at shallow depths near the receivers. Given the crustal heterogeneity common in seismically active areas, such a model might appear plausible. However, in principle this idea can be tested by checking whether stacks for stations near earthquake source regions appear significantly different than those from stations in tectonically stable areas. Tests we performed for several stations in active and inactive regions do not support such a difference.

(ii) Shallow or deep earthquakes might radiate different amounts of high-frequency shear wave energy than standard theory predicts, either as part of the main shock rupture process or by triggering early aftershocks in the first few minutes following the event. Scattering from these *S* waves is a significant contributor to *P* coda. In fact, it has been observed (e.g. Boatwright & Fletcher 1984; Abercrombie 1995) that *P*-wave corner frequencies are somewhat higher than *S*-wave corner frequencies and that radiated *S* energy is between 9 and 17 times larger than radiated *P* energy, significantly less than the value of 23.4 that we used. Thus, it appears possible that our method may overestimate the S/P energy ratio at 1 Hz.

(iii) Scattering near shallow-earthquake source regions could involve non-linear or time-dependent effects. For example, if strong shaking created or opened cracks, this could enhance scattering and reverberations near the source for a limited time period until the cracks healed.

(iv) Our modelling method might not include some critical part of Earth properties. One possibility is directional scattering caused by upper-mantle anisotropy (or crustal and/or upper-mantle waveguides). Properly testing these possibilities is, however, well beyond the scope of this paper.

It may be possible to discriminate among these ideas by examining local and regional coda data, as well as the teleseismic records that we consider here. In addition, we have only attempted to model the *P* coda in this paper; our synthetics predict scattering of other phases, such as *PKP*, which provide further constraints on suitable models. We plan to examine *PKP* scattering in a future study to help resolve the discrepancy in inferred lower-mantle heterogeneity between the Hedlin *et al.* (1997) and Margerin & Nolet (2003b) studies. It would also be useful to begin computing coda stacks in different frequency bands: this would help to resolve the scatterer size distribution in more detail than is possible here.

6 CONCLUSIONS

We have attempted to derive first-order, self-consistent models of scattering in the Earth that can explain the gross features that are seen in the high-frequency wavefield. To this end, we have applied a stacking procedure to global seismic data to produce images of average *P* coda amplitude as a function of distance and time. To model these results, we have developed and tested a Monte Carlo seismic phonon method suited for modelling high-frequency scattering at all Earth depths. Our method can handle both *P* and *S* waves (including *S* polarizations), model discontinuities and intrinsic attenuation. Tests of the method for simple whole-space scattering yield results that agree with theoretical predictions. We are able to achieve reasonable fits to the data stacks with fairly simple models of whole-mantle heterogeneity. Our results suggest that most scattering occurs in the lithosphere and upper mantle, as previous results have indicated, but that some lower-mantle scattering is likely also required.

ACKNOWLEDGMENTS

This research was supported by National Science Foundation grants EAR9909267 and EAR0229323. The authors thank John Vidale and an anonymous reviewer for many helpful suggestions.

REFERENCES

Abercrombie, R.E., 1995. Earthquake source scaling relationships from −1 to 5 M_L using seismograms recorded at 2.5-km depth, *J. geophys. Res.,* **100,** 24 015–24 036.

Aki, K., 1969. Analysis of seismic coda of local earthquakes as scattered waves, *J. geophys. Res.,* **74,** 615–631.

Aki, K. & Chouet, B., 1975. Origin of coda waves: source attenuation and scattering effects, *J. geophys. Res.,* **80,** 3322–3342.

Astiz, L., Earle, P. & Shearer, P., 1996. Global stacking of broadband seismograms, *Seismol. Res. Lett.* **67,** 8–18.

Bhattacharyya, J., Shearer, P. & Masters, G., 1993. Inner core attenuation from short-period *PKP*(*BC*) versurs *PKP*(*DF*) waveforms, *Geophys. J. Int.,* **114,** 1–11.

Boatwright, J. & Fletcher, J.B., 1984. The partition of radiated seismic energy between *P* and *S* waves, *Bull. seism. Soc. Am.,* **74,** 361–376.

Cleary, J.R. & Haddon, R.A.W., 1972. Seismic wave scattering near the core-mantle boundary: a new interpretation of precursors to *PKP*, *Nature,* **240,** 549–551.

Earle, P.S. & Shearer, P.M., 1997. Observations of *PKKP* precursors used to estimate small-scale topography on the core-mantle boundary, *Science,* **277,** 667–670.

Earle, P.S. & Shearer, P.M., 2001. Distribution of fine-scale mantle heterogeneity from observations of Pdiff coda, *Bull. seism. Soc. Am.,* **91,** 1875–1881.

Frankel, A. & Wennerberg, L., 1987. Energy-flux model of seismic coda: separation of scattering and intrinsic attenuation, *Bull. seism. Soc. Am.,* **77,** 1223–1251.

Gusev, A.A. & Abubakirov, I.R., 1987. Monte-Carlo simulation of record envelope of a near earthquake, *Phys. Earth. planet. Int.,* **49,** 30–36.

Gusev, A.A. & Abubakirov, I.R., 1996. Simulated envelopes of non-isotropically scattered body waves as compared to observed ones: another manifestation of fractal heterogeneity, *Geophys. J. Int.,* **127,** 49–60.

Hedlin, M.A.H. & Shearer, P.M., 2000. An analysis of large-scale variation in small-scale mantle heterogeneity using Global Seismographic Network recordings of precursors to *PKP*, *J. geophys. Res.,* **105,** 13 655–13 673.

Hedlin, M.A.H., Shearer, P.M. & Earle, P.S., 1997. Seismic evidence for small-scale heterogeneity throughout Earth's mantle, *Nature,* **387,** 145–150.

Hoshiba, M., 1991. Simulation of multiple-scattered coda wave excitation based on the energy conservation law, *Phys. Earth. planet. Int.,* **67,** 123–136.

Hoshiba, M., 1994. Simulation of coda wave envelope in depth dependent scattering and absorption structure, *Geophys. Res. Lett.,* **21,** 2853–2856.

Hoshiba, M., 1997. Seismic coda wave envelope in depth-dependent S wave velocity structure, *Phys. Earth. planet. Int.,* **104,** 15–22.

Kanasewich, E.R., 1981. *Time sequence analysis in geophysics* University of Alberta Press, Edmonton, AB, Canada.

Korn, M., 1990. A modified energy flux model for lithospheric scattering of teleseismic body waves, *Geophys. J. Int.,* **102,** 165–175.

Korn, M., 1993. Determination of site-dependent scattering *Q* from *P*-wave coda analysis with an energy flux model, *Geophys. J. Int.,* **113,** 54–72.

Korn, M., 1997. Modelling the teleseismic P coda envelope: depth dependent scattering and deterministic structure, *Phys. Earth. planet. Int.,* **104,** 23–36.

Lee, W.S., Sato, H. & Lee, K., 2003. Estimation of S-wave scattering coefficient in the mantle from envelope characteristics before and after the ScS arrival, *Geophys. Res. Lett.,* **30**(24), 2248, doi:10.1029/2003GL018413.

Margerin, L. & Nolet, G., 2003a. Multiple scattering of high-frequency seismic waves in the deep Earth: Modeling and numerical examples, *J. geophys. Res.,* **108**(B5), 2234, doi:10.1029/2002JB001974.

Margerin, L. & Nolet, G., 2003b. Multiple scattering of high-frequency seismic waves in the deep Earth: PKP precursor analysis and inversion for mantle granularity, *J. geophys. Res.,* **108**(B11), 2514, doi:10.1029/2003JB002455.

Margerin, L., Campillo, M. & Tiggelen, B.V., 2000. Monte Carlo simulation of multiple scattering of elastic waves, *J. geophys. Res.,* **105,** 7873–7892.

Saito, T., Sato, H., Fehler, M. & Ohtake, M., 2003. Simulating the envelope of scalar waves in 2D random media having power-law spectra of velocity fluctuation, *Bull. seism. Soc. Am.,* **93,** 240–252.

Sato, H., 1984. Attenuation and envelope formation of three-component seismograms of small local earthquakes in randomly inhomogeneous lithosphere, *J. geophys. Res.,* **89,** 1221–1241.

Sato, H., 1991. Study of seismogram envelopes based on scattering by random inhomogeneities in the lithosphere: a review, *Phys. Earth. planet. Int.,* **67,** 4–19.

Sato, H. & Fehler, M.C., 1998. *Seismic Wave Propagation and Scattering in the Heterogeneous Earth,* Springer-Verlag, New York (S&F).

Veith, K.F. & Clawson, G.E., 1972. Magnitude from short-period P-wave data, *Bull. seism. Soc. Am.,* **62,** 435–452.

Wagner, G.S. & Langston, C.A., 1992. A numerical investigation of scattering effects for teleseismic plane wave propagation in a heterogeneous layer over a homogeneous half-space, *Geophys. J. Int.,* **110,** 486–500.

Warren, L.M. & Shearer, P.M., 2000. Investigating the frequency dependence of mantle Q by stacking P and PP spectra, *J. geophys. Res.,* **105,** 25 391–25 402.

Wu, R.-S., 1985. Multiple scattering and energy transfer of seismic waves–separation of scattering effect from intrinsic attenuation–I. Theoretical modelling, *Geophys. J. R. astr. Soc.,* **82,** 57–80.

Wu, R. & Aki, K., 1985a. Scattering characteristics of elastic waves by an elastic heterogeneity, *Geophysics,* **50,** 582–595.

Wu, R. & Aki, K., 1985b. Elastic wave scattering by a random medium and the small-scale inhomogeneities in the lithosphere, *J. geophys. Res.,* **90,** 10 261–10 273.

Yoshimoto, K., 2000. Monte Carlo simulation of seismogram envelopes in scattering media, *J. geophys. Res.,* **105,** 6153–6161.

Zheng, Y., 1991. Compact solutions for multiple scattered wave energy in the time domain, *Bull. seism. Soc. Am.,* **81,** 1022–1029.